

Probing the interlayer coupling in $2H\text{-NbS}_2$ via soft-x-ray angle-resolved photoemission spectroscopy

D. Huang,^{1,*} H. Nakamura,^{2,†} K. Küster,¹ U. Wedig,¹ N. B. M. Schröter,^{3,‡} V. N. Strocov,³ U. Starke,¹ and H. Takagi^{1,4,5}

¹Max Planck Institute for Solid State Research, 70569 Stuttgart, Germany

²Department of Physics, University of Arkansas, Fayetteville, Arkansas 72701, USA

³Swiss Light Source, Paul Scherrer Institute, CH-5232 Villigen PSI, Switzerland

⁴Institute for Functional Matter and Quantum Technologies, University of Stuttgart, 70569 Stuttgart, Germany

⁵Department of Physics, University of Tokyo, 113-0033 Tokyo, Japan

(Dated: July 1, 2022)

In the large family of two-dimensional (2D) layered materials including graphene, its honeycomb analogs, and transition-metal dichalcogenides, the interlayer coupling plays a rather intriguing role. On the one hand, the weak van der Waals interaction that holds the layers together endows these compounds with quasi-2D properties, which might imply small interlayer effects on the electronically active bands. On the other hand, the oft-witnessed differences in electronic, optical, and magnetic behaviors of monolayers, bilayers, and multilayers of the same compound must have as their microscopic origin the detailed interlayer hopping parameters. Given the few experimental reports that have attempted to explicitly extract these parameters, we employ soft-x-ray angle-resolved photoemission spectroscopy (SX-ARPES) to probe the interlayer coupling in superconducting $2H\text{-NbS}_2$. We visualize the $S\ 3p_z$ bands that disperse with respect to the out-of-plane momentum and introduce a simple tight-binding model to extract the interlayer hopping parameters. From first-principles calculations, we clarify how atomic distances and the proper accounting for screening via hybrid functionals influence these bands. The knowledge of interlayer hopping parameters is particularly pertinent in NbS_2 , where recent experiments have uncovered fingerprints of finite-momentum superconductivity in the bulk material and heterostructures.

I. INTRODUCTION

The broad class of van der Waals (vdW) materials consisting of two-dimensional (2D) atomic layers weakly bonded in the third dimension continues to fuel intense research activity. The ability to isolate monolayers with properties that are sharply distinct from the bulk is particularly appealing. For example, when a single sheet of graphene is exfoliated from graphite, a 2D Dirac semimetal with zero band gap is obtained [1]. When semiconducting MoS_2 is thinned down to a monolayer, the band gap changes from indirect to direct [2]. A bilayer of CrI_3 is antiferromagnetic, but a monolayer (or an odd number of layers) is ferromagnetic [3]. Bulk $T_d\text{-WTe}_2$ is a type-II Weyl semimetal, whereas monolayer $T'\text{-WTe}_2$ is a 2D topological insulator [4, 5].

The microscopic origin of these layer-dependent properties is the intricate interlayer coupling in vdW materials. Fundamentally, the problem reduces to deriving universal and transferable forms of interlayer hopping, for example, between the chalcogen p_z orbitals of transition-metal dichalcogenides (TMDCs) [6, 7] or the C $2p_z$ -like orbitals of graphite [8], that depend only on the relative distance and orientations of the orbitals. These interlayer

hopping formulas yield predictive power for the stacking of different monolayers to form heterostructures, or with a twist angle between the respective lattices [8, 9]. While numerical values for these formulas can be extracted from density functional theory (DFT) calculations, two challenges exist: First, the common approximations to the exchange-correlation functional fail to capture the vdW forces that crucially determine the interlayer distances in these compounds. Second, real materials often suffer from atomic and stacking defects that also affect the average interlayer distance. Hence, experimental means of directly probing the interlayer coupling are highly desirable.

Angle-resolved photoemission spectroscopy (ARPES) is a powerful technique for visualizing band structures. Signatures of interlayer coupling may be detected and quantified through additional splitting or gapping of the band structure compared to that of the single layer, or by tracing the band dispersion with respect to the out-of-plane momentum k_z [10–13]. In the latter case, one must note that in the photoemission process, only the in-plane momentum is conserved, and k_z must be inferred assuming a free-electron-like final state and controlled by tuning the incoming photon energy. In this regard, the use of soft-x-ray (SX) photons generated by a synchrotron confers two advantages over the use of conventional vacuum-ultraviolet photons [14]: First, the higher photon energy (up to 1–2 keV) results in a larger photoelectron escape depth λ , and in turn, smaller uncertainty in k_z ($\delta k_z = \lambda^{-1}$, where δk_z is the full width at half

* D.Huang@fkf.mpg.de

† hnakamur@uark.edu

‡ Present address: Max Planck Institute for Microstructure Physics, 06120 Halle, Germany

maximum [15]). Second, the higher energy of the final state means that the free-electron approximation works better. One limitation in extracting the interlayer coupling from the k_z dispersion is that the system must be 3D or sufficiently thick; this method would not apply to bilayer or few-layer vdW materials.

For a model vdW system to explore interlayer coupling, we turn to the superconducting TMDC $2H$ - NbS_2 [crystal structure shown in Fig. 1(a)]. NbS_2 is iso-electronic to its more-studied counterpart NbSe_2 , and even has a similar superconducting transition temperature ($T_c \approx 6$ K compared to 7 K [16]), yet possesses a few distinct and curious features. The coexisting charge density wave (CDW) phase present in NbSe_2 is absent in NbS_2 [17–20], though vestiges may be pinned to defect structures [21, 22]. Theoretical studies point to NbS_2 hosting stronger many-body effects than NbSe_2 , including competing Coulomb and electron-phonon interactions, and lying on the verge of instability to charge or even spin ordering [23–29]. Most surprisingly, when a magnetic field is carefully aligned parallel to the NbS_2 layers, the upper critical field shows an upturn above the Pauli limit, reminiscent of the Fulde-Ferrell-Larkin-Ovchinnikov state with finite-momentum Cooper pairs [30]. However, Ising spin-orbit coupling in TMDC monolayers may provide an alternative means for the system to exceed the Pauli limit, and one deciding factor is the dimensionality of bulk NbS_2 ; i.e., how strong the individual layers are coupled. In this respect, mapping the 3D band structure is foundational.

Here, we report SX-ARPES measurements of NbS_2 taken at the ADDRESS beamline of the Swiss Light Source [31, 32]. By tuning the photon energy, we could observe the S $3p_z$ bands that disperse with respect to k_z . We model the k_z dispersion by an effective tight-binding (TB) model, through which the interlayer hopping parameters could be extracted. Extensive DFT calculations elucidate the role of structural parameters and hybrid functionals in reproducing the experimentally observed bands.

II. RESULTS

A. Transport

Figures 1(b) and 1(c) show resistivity vs. temperature plots of a NbS_2 single crystal. Upon cooling, the resistivity exhibits a smooth decrease with no kinks, indicating the absence of a CDW transition in NbS_2 . At $T_c = 5.4$ K, a superconducting transition is observed. While the T_c is comparable to literature values, the residual resistivity ratio (RRR) of 11 is slightly lower than that of cleaner single crystals (RRR ≈ 20 [33] and 70 [22]) and comparable to samples that may be slightly deficient of S [34]. X-ray photoelectron spectroscopy (XPS) measurements revealed an excess of Nb in our samples. These Nb atoms intercalate the vdW gap and create two distinct

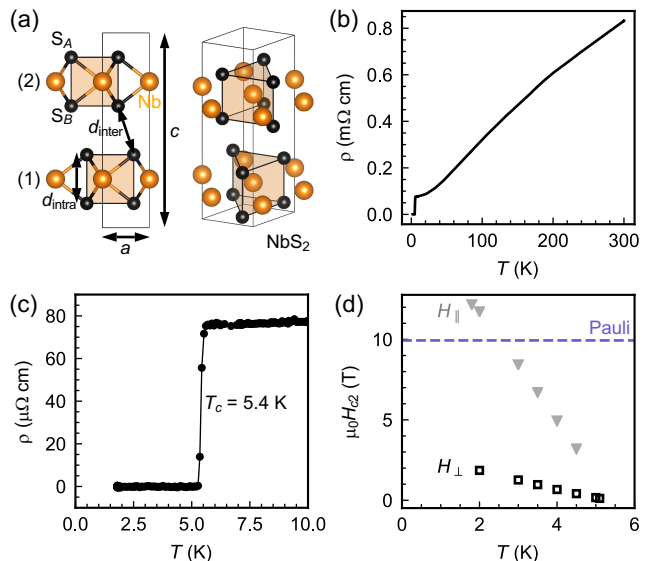


FIG. 1. (a) Crystal structure and definition of structural parameters. The numbers (1) and (2) and the subscript letters A and B are used in the construction of the TB model [Eq. (2)]. (b) Resistivity vs. temperature from 300 to 1.8 K. (c) Magnification of (b) around the superconducting transition. (d) In-plane (\parallel) and out-of-plane (\perp) upper critical fields vs. temperature. The former surpasses the theoretical Pauli limit around 2 K.

crystallographic sites for S, evident as two components in the S $2p$ core levels [35, 36]. Figure 1(d) demonstrates the anisotropy between the in-plane and out-of-plane upper critical fields (H_{c2}). At 2 K, the ratio $H_{c2,\parallel}/H_{c2,\perp} \approx 6.3$ is similar to reported values of 7.5–8 for NbS_2 and larger than reported values of 2.3–3.2 for NbSe_2 [37]. $H_{c2,\parallel}$ also exceeds the Pauli limit of $1.84 T_c$, as previously reported and discussed [30].

B. SX-ARPES

We begin our discussion of the SX-ARPES results by presenting intensity cuts that span the high symmetry points of the Brillouin zone. Figures 2(a)–2(c) show cuts along the in-plane momentum k_{\parallel} at three different photon energies, $h\nu = 407, 590,$ and 566 eV, corresponding to $k_z = 0, 0,$ and π/c , where c is the length of the unit cell perpendicular to the layers [Fig. 1(a)]. Circularly polarized photons were used, in order to visualize both orbitals that are odd and even with respect to the k_x - k_z plane [35, 38, 39]. The inset of Fig. 2(a) shows a cut of the Fermi surface at $k_z = 0$, comprising pockets centered at Γ and K . As marked by the gray shaded regions in Figs. 2(b) and 2(c), these pockets have hole-like nature and extend to the A and H points at $k_z = \pi/c$, where according to DFT calculations, the pockets are doubly degenerate. Our results show good agreement with previous ARPES reports of NbS_2 probing its

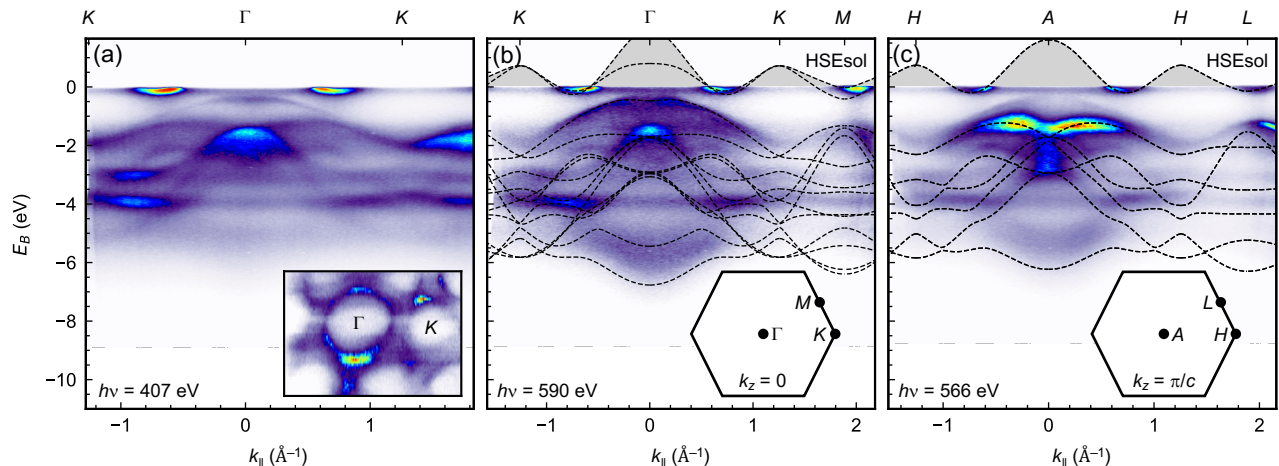


FIG. 2. In-plane band dispersion of $2H$ - NbS_2 . (a) and (b) SX-ARPES intensity cuts in the $k_z = 0$ plane at two photon energies, $h\nu = 407$ and 590 eV. Inset of (a): Fermi surface in the $k_z = 0$ plane, visualized by integrating within the binding energy (E_B) window $[-100 \text{ meV}, 100 \text{ meV}]$; $h\nu = 407$ eV. A slight artificial distortion is present, due to the cleaved surface exhibiting small flakes and domains with different tilt angles and the challenge of maintaining the beam spot on the same area while tilting the sample platform. (c) SX-ARPES intensity cut in the $k_z = \pi/c$ plane; $h\nu = 566$ eV. In (b) and (c), DFT calculations (HSEsol functional) are overlaid as dashed lines, and the gray-shaded regions mark hole pockets that intersect E_F . Insets of (b) and (c): Brillouin zone in the $k_z = 0$ and π/c planes.

2D band dispersion [26, 40, 41]. However, we observe a holelike band at Γ , just below the Fermi energy (E_F), which was absent in the data of Refs. [26, 40], taken at $h\nu = 40$ eV. This band was later detected in Ref. [41] at $h\nu = 79$ eV, but without the full k_z dispersion from 0 to π/c . From DFT calculations, this band comprises S $3p_z$ orbitals, and its k_z dispersion will play a central role in the ensuing discussion of interlayer coupling.

We turn our attention to the k_z evolution of the band structure along the Γ - A line. As seen in Fig. 3(a) [and more clearly visualized in the second derivative plot; Fig. 3(b)], there are two pairs of k_z -dispersive bands centered around -1.75 and -5 eV, which should be intimately related to the interlayer coupling, and two sets of k_z -nondispersive bands around -1.5 and -2.5 eV, which are 2D in nature. The k_z -dispersive bands exhibit twice the periodicity of the unit cell, an effect which can be attributed to matrix-element effects due to the $2H$ structure with two NbS_2 layers per unit cell [39]. The k_z -dispersive bands also show secondary replicas shifted in k_z [marked by red arrows in Fig. 3(b)], which arise because the final state is not a pure free electron and therefore contains an admixture of other k_z values [42]. In spite of these artifacts, the existence of both the k_z -dispersive and k_z -nondispersive bands is reproduced by DFT calculations [overlaid in Fig. 3(a)]. The pair of k_z -dispersive bands closer to E_F comprises S $3p_z$ orbitals in an odd combination with respect to the Nb plane, while the other pair of k_z -dispersive bands deep below E_F includes both S $3p_z$ orbitals in an even combination and Nb $4d_{z^2}$ orbitals. The k_z -nondispersive bands closer to E_F comprise four odd combinations of S $3p_{x/y}$ and

Nb $4d_{xz/yz}$ orbitals with respect to the Nb plane, while the k_z -nondispersive bands further below E_F include four even combinations of S $3p_{x/y}$ and Nb $4d_{xy/x^2-y^2}$ orbitals. These orbital assignments are consistent with the photon polarization dependence of their ARPES intensities [35].

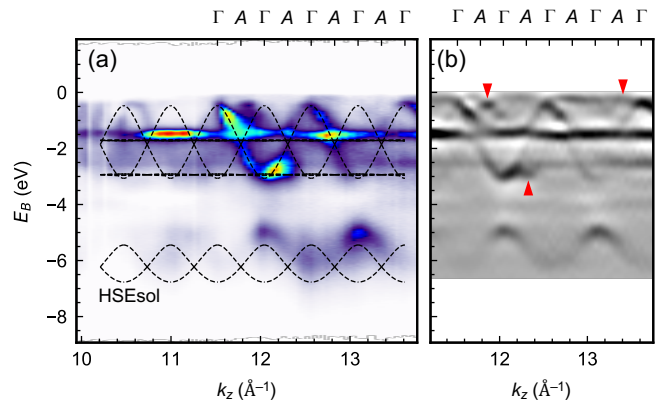


FIG. 3. Out-of-plane band dispersion of $2H$ - NbS_2 . (a) SX-ARPES intensity as a function of k_z , tuned by the photon energy, along the Γ - A line ($k_{\parallel} = 0$). DFT calculations (HSEsol functional) are overlaid as dashed lines. (b) Second-derivative image of (a). The red arrows mark replica bands.

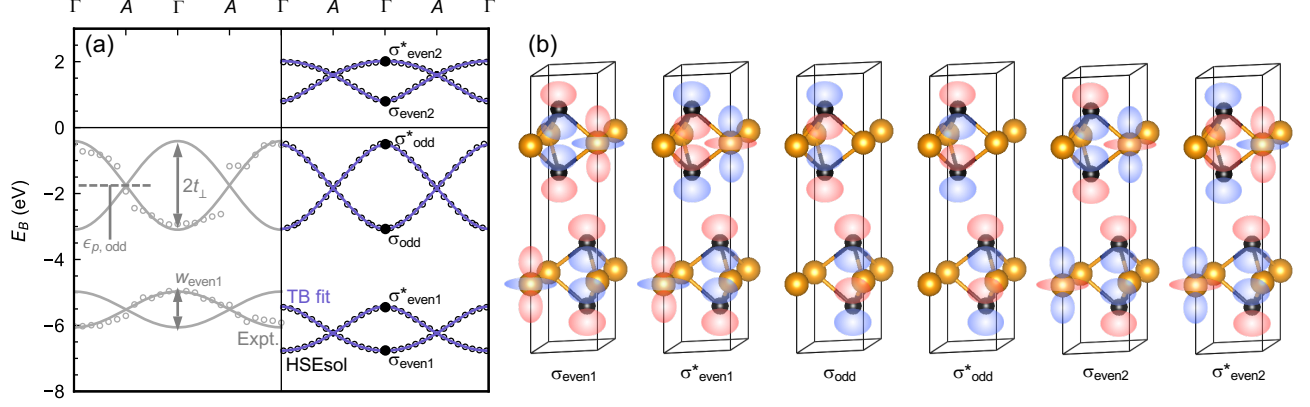


FIG. 4. Effective model for k_z -dispersive bands. (a) Band dispersion along Γ -A derived from experiment (left), DFT (open circles; HSEsol hybrid functional; right), and a TB fit to DFT (line; Eq. (2); right). (b) Schematic orbital compositions of the states at Γ . Red and blue colors denote the phases of the lobes. The odd orbitals S $3p_{z,\text{odd}}$ form one pair of bonding and antibonding states, σ_{odd} , σ_{odd}^* , whereas the even orbitals S $3p_{z,\text{even}}$ and Nb $4d_{z^2}$ form two pairs of bonding and antibonding states, σ_{even1} , σ_{even1}^* and σ_{even2} , σ_{even2}^* .

C. Effective TB Model for k_z -dispersive bands

The relative simplicity of the k_z -dispersive bands in Fig. 3 motivates the construction of an effective TB model restricted to the Γ -A line ($k_{\parallel} = 0$). We first take a single NbS₂ layer with the $4d_{z^2}$ orbital of the Nb atom and the $3p_z$ orbitals of the two S atoms. Since there is mirror symmetry with respect to the Nb plane, the S $3p_z$ orbitals can be expressed as odd and even combinations that do not mix: $p_{z,\text{odd}} = (p_{z,A} + p_{z,B})/\sqrt{2}$ and $p_{z,\text{even}} = (p_{z,A} - p_{z,B})/\sqrt{2}$, where $p_{z,A}$ and $p_{z,B}$ are orbitals for the S atoms above and below the Nb plane, respectively [7]. Next, we consider the full unit cell with two NbS₂ layers [labeled (1) and (2) in Fig. 1(a)]. Our

basis is thus

$$\psi^\dagger = (p_{z,\text{odd}}^{(1)\dagger}, p_{z,\text{even}}^{(1)\dagger}, d_{z^2}^{(1)\dagger}, p_{z,\text{odd}}^{(2)\dagger}, p_{z,\text{even}}^{(2)\dagger}, d_{z^2}^{(2)\dagger}). \quad (1)$$

Within each layer, the $p_{z,\text{odd}}$, $p_{z,\text{even}}$, and d_{z^2} orbitals have energies $\epsilon_{p,\text{odd}}$, $\epsilon_{p,\text{even}}$, and ϵ_d , respectively. We further posit that the only interlayer hopping is between neighboring pairs $p_{z,A}^{(1)} - p_{z,B}^{(2)}$ and $p_{z,B}^{(1)} - p_{z,A}^{(2)}$, denoted by t_{\perp} , and that the only intralayer hybridization allowed by symmetry is between the even orbitals $p_{z,\text{even}}$ and d_{z^2} orbitals, denoted by t_{\parallel} . We arrive at the following 6×6 Hamiltonian matrix describing the k_z dispersion along Γ -A:

$$H_{\text{eff}}(k_z) = \begin{pmatrix} \epsilon_{p,\text{odd}} & 0 & 0 & t_{\perp} \cos(\frac{k_z c}{2}) & it_{\perp} \sin(\frac{k_z c}{2}) & 0 \\ 0 & \epsilon_{p,\text{even}} & t_{\parallel} & -it_{\perp} \sin(\frac{k_z c}{2}) & -t_{\perp} \cos(\frac{k_z c}{2}) & 0 \\ 0 & t_{\parallel} & \epsilon_d & 0 & 0 & 0 \\ t_{\perp} \cos(\frac{k_z c}{2}) & it_{\perp} \sin(\frac{k_z c}{2}) & 0 & \epsilon_{p,\text{odd}} & 0 & 0 \\ -it_{\perp} \sin(\frac{k_z c}{2}) & -t_{\perp} \cos(\frac{k_z c}{2}) & 0 & 0 & \epsilon_{p,\text{even}} & t_{\parallel} \\ 0 & 0 & 0 & 0 & t_{\parallel} & \epsilon_d \end{pmatrix}. \quad (2)$$

Fig. 4(a) (right half) shows the six bands computed from Eq. 2. When $k_z = 0$, the eigenvalues can be solved analytically (see Appendix B) and the orbital compositions of the eigenstates are simple [Fig. 4(b)]. The S $3p_{z,\text{odd}}$ orbitals form bonding and antibonding combinations with respect to the vdW gap, σ_{odd} , σ_{odd}^* , with average energy $\epsilon_{p,\text{odd}}$ and bandwidth $w_{\text{odd}} = 2t_{\perp}$. Comparison with experiment yields $t_{\perp} = 1.34$ eV and $\epsilon_{p,\text{odd}} = -1.75$ eV (Fig. 4(a); left half). The even orbitals S $3p_{z,\text{even}}$ and Nb $4d_{z^2}$ hybridize and produce two pairs

of bonding and antibonding states, σ_{even1} , σ_{even1}^* and σ_{even2} , σ_{even2}^* . If there were no hybridization, the bandwidths of the independent pairs of $p_{z,\text{even}}$ and d_{z^2} bands would have been $2t_{\perp}$ and zero, respectively. With sizeable hybridization, the bandwidths are given approximately by

$$w_{\text{even1}}, w_{\text{even2}} \approx t_{\perp} [1 \mp (\epsilon_{p,\text{even}} - \epsilon_d)/(2t_{\parallel})]. \quad (3)$$

From experiment, we extract $w_{\text{even1}} = 1.09$ eV, whereas w_{even2} is inaccessible because σ_{even2} , σ_{even2}^* lie above E_F .

D. Comparison with DFT

Since only four of the six bands lie below E_F , a full fit of the experimental data to Eq. (2) with five parameters is underconstrained, and we cannot uniquely determine the experimental values of $\epsilon_{p,\text{even}}$, ϵ_d , and t_{\parallel} . To estimate these parameters, we fit Eq. (2) to DFT calculations, an example of which is shown in Fig. 4(a) (right half). Given previous reports emphasizing the use of vdW, GW , and other many-body corrections in modeling NbS₂ [25–27, 41, 47], we explore a range of functionals in Figs. 5(a)–5(f): the standard Perdew-Burke-Ernzerhof (PBE) parametrization [48] of the generalized gradient approximation, the Heyd-Scuseria-Ernzerhof (HSE06) short-range separated hybrid functional [49], and the corresponding functionals revised for solids (PBEsol [50], HSEsol [51]). VdW interactions were taken into account by adding dispersion terms according to the D3 method [52] to the DFT energies (PBE+D3, HSE06+D3, PBEsol+D3, HSEsol+D3). For each calculation, we perform full structural relaxation, since literature values exhibit some ambiguity (Refs. [43–46]; see Supplementary Table 4). Values for the c lattice constant and intralayer and interlayer S-S distances (d_{intra} , d_{inter}) are plotted in Figs. 5(g)–5(i).

In Fig. 5, we can understand the variation in the c -axis parameter as follows: PBE and HSE06, which are based on the same exchange functional without and with admixture of Hartree-Fock exchange, miss the vdW interactions and underbind the NbS₂ layers, leading to larger c . PBEsol and HSEsol perform reasonably in estimating c . The D3 corrections overbind the NbS₂ layers, leading to smaller c . Interestingly, d_{intra} remains relatively constant, whereas d_{inter} varies according to c . However, it should be noted that the potential energy surface is very flat along c , and for a wide range of d_{inter} , the total energy varies only by roughly 30 meV [35].

From Fig. 5, we can also determine which TB parameters are sensitive to atomic positions, which TB parameters are sensitive to the screening in the hybrid functionals, and which TB parameters are sensitive to both. The interlayer hopping t_{\perp} [Fig. 5(c)] and bandwidth $w_{\text{even}1}$ [Fig. 5(f)] show the greatest variation across calculations and vary inversely proportional to c [Fig. 5(g)] and d_{inter} [Fig. 5(h)], as expected. On the other hand, $\epsilon_{p,\text{odd}}$ and t_{\parallel} are bimodal, adopting one value for PBE functionals, and another for hybrid functionals [red arrows and bars in Figs. 5(b) and 5(e)], with little dependence on c . The parameter $\epsilon_{p,\text{even}}$ [Fig. 5(a)] shows moderate variation directly proportional to c , whereas ϵ_d [Fig. 5(d)] is influenced by both c and hybrid functionals. Although we might expect the intralayer terms to be insensitive to interlayer distances, two factors could account for the observed c -dependence of $\epsilon_{p,\text{even}}$ and t_{\parallel} : First, intralayer hopping is indirectly affected by the c lattice constant through concomitant changes in the a lattice constant. Second, there is an additional interlayer hopping channel between the S $3p_z$ and Nb $4d_{z^2}$ orbitals, which is sensitive

to c . These effects may be buried in $\epsilon_{p,\text{even}}$ and t_{\parallel} .

III. DISCUSSION

The extraction of interlayer hopping parameters in this work hinges upon the SX-ARPES data with k_z dependence. In previous ARPES measurements of NbS₂ acquired at a fixed photon energy [26, 40, 41], the corresponding value of k_z was unknown. Furthermore, due to matrix element effects, the $\sigma_{\text{even}2}$, $\sigma_{\text{even}2}^*$ bands needed to estimate t_{\perp} are visible at different photon energies. For example, the $\sigma_{\text{even}2}^*$ band was not detected at $h\nu = 40$ eV.

By visual inspection of previously reported SX-ARPES data of TMDC compounds with Se, we can similarly estimate the interlayer hopping t_{\perp} between overlapping Se $4p_z$ orbitals to be roughly 1.3–1.4 eV in $2H$ -NbSe₂ [39] and 1.5 eV in $1T$ -VSe₂ [14]. While the larger size of the Se $4p_z$ orbitals compared to the S $3p_z$ orbitals would increase interlayer coupling, a larger d_{inter} would decrease interlayer coupling, but d_{inter} is difficult to determine precisely: 3.22–3.56 Å for NbS₂ [43–46], compared to 3.53–3.55 Å for NbSe₂ [53, 54] and 3.52–3.56 Å for VSe₂ [55, 56]. In any case, the interlayer hopping in these TMDCs is larger than the value of 0.35–0.48 eV observed in few-layer graphene and graphite [11]. This does not necessarily imply that graphite is electronically more 2D than the TMDCs. In the former, the same C $2p_z$ -like orbitals that form the π bands intersecting E_F also constitute the primary channel of interlayer hopping. In the latter, multiple bands with both transition metal d and chalcogen p characters lie near E_F , but there is only significant interlayer hopping through the p_z orbitals. The relative weight of p_z orbitals in the composition of the Fermi surface is an additional factor that determines the electronic dimensionality of TMDCs.

Overall, with respect to the σ_{odd} , σ_{odd}^* bands closest to E_F , the HSEsol calculation best reproduces the experimental NbS₂ data and is shown in Figs. 2(b), 2(c), 3(a), and 4(a), together with the experimental data. In particular, the HSEsol calculation correctly predicts the band maximum of σ_{odd}^* lying 0.4 eV below E_F . Previous calculations with PBE, GW corrections, and/or vdW corrections either predict this band crossing E_F and forming an additional hole pocket at Γ , or lying barely below E_F [25, 26, 47]. The implications on superconducting properties are as follows: Calculations of T_c using DFT band structures with a σ_{odd}^* Fermi pocket overestimate the density of states around E_F and exceed the experimental T_c by a factor of 2–3 [25]. Our results may yield improved estimates of T_c . The absence of S $3p_z$ states with strong k_z dispersion at E_F also causes the Fermi surface to be more 2D, which may contribute to the observed enhancement of the in-plane upper critical field, as orbital depairing is suppressed. In contrast, the Se $4p_z$ states form a small 3D pocket in NbSe₂ [39], which may partly explain the reduced anisotropy in its upper criti-

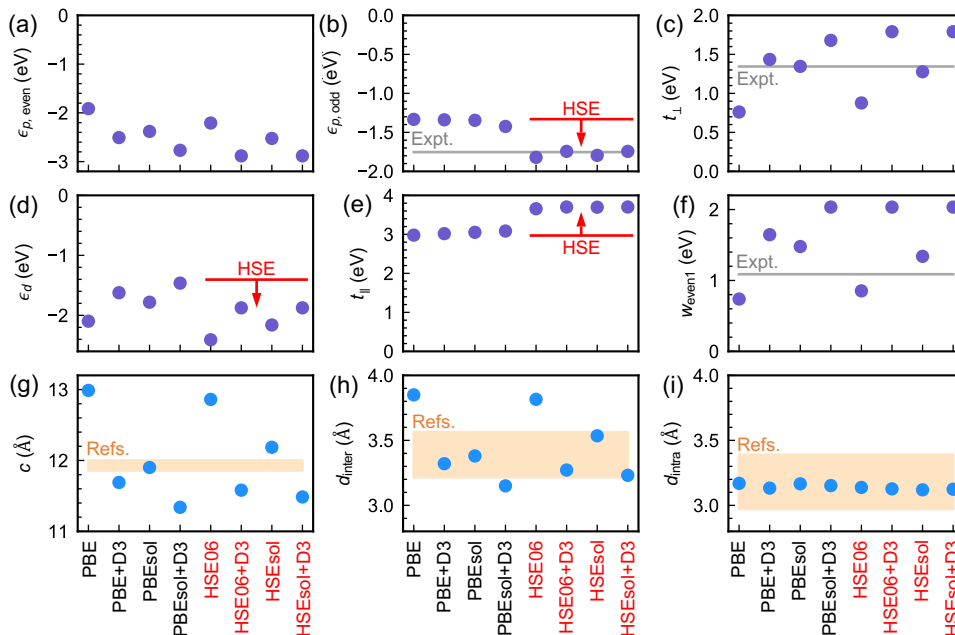


FIG. 5. Benchmark of DFT methods against interlayer coupling in NbS₂. (a)–(f) TB parameters derived from fits of Eq. (2) to DFT calculations with various exchange-correlation and hybrid functionals. Experimental values are depicted as gray horizontal lines. The red horizontal lines and arrows denote a systematic offset introduced by hybrid functionals. (g)–(i) Optimized structural parameters corresponding to the DFT calculations. The shaded orange regions represent the spread of structural parameters reported in Refs. [43–46]. The intralayer S-S distance (d_{intra}) and the interlayer S-S distance (d_{inter}) are defined in Fig. 1(a).

cal field. Our results also suggest an avenue to raising T_c in NbS₂ by applying uniaxial pressure along the c -axis, which enhances the interlayer hopping t_{\perp} and pushes the band maximum of σ_{odd}^* closer to E_F .

Nevertheless, the HSEsol calculation does not perform as well in reproducing the σ_{even1} , σ_{even1}^* bands and the k_z -nondispersive bands [Fig. 3(a)]. More sophisticated theoretical techniques, such as dynamical mean-field theory, could provide one remedy [57]. Alternatively, these discrepancies may arise from the presence of defects in real materials. $2H$ -NbS₂ and related compounds are prone to stacking faults, polytypism, Nb intercalants, and S vacancies, which sensitively affect the structural and hence interlayer hopping parameters [21, 22, 34]. In our SX-ARPES data, we note some faint flat bands (e.g., around -4 eV in Fig. 2) that may be defect levels [40]. The RRR value of 11 and XPS measurements of core S $2p$ levels [35] also corroborate the presence of defects – specifically, Nb intercalants. Thus, direct experimental probes of interlayer coupling are useful in these scenarios.

IV. CONCLUSION

We have utilized SX-ARPES to probe the interlayer coupling of superconducting $2H$ -NbS₂. The extraction of interlayer hopping parameters is aided by the use of an effective TB model, which also facilitates the comparison with DFT calculations using various functionals. An

interesting extension of our work would be to measure the k_z dispersion in superlattice heterostructures with monolayer NbS₂ separated by buffer layers, realized either through misfit compounds [58] or thin films. Such structures hold promise for realizing exotic superconductivity in the presence of an in-plane magnetic field, and the interlayer coupling between NbS₂ layers is a key parameter.

ACKNOWLEDGMENTS

We thank K. Pflaum for technical support. We acknowledge the Paul Scherrer Institut, Villigen, Switzerland, for provision of synchrotron radiation beam time at the ADDRESS beamline of the Swiss Light Source. D.H. acknowledges support from a Humboldt Research Fellowship for Postdoctoral Researchers. N.B.M.S. acknowledges partial financial support from Microsoft.

APPENDIX A: METHODS

Superconducting single crystals of $2H$ -NbS₂ were purchased from 2D Semiconductors. Resistivity measurements in the standard four-probe configuration were performed in a physical property measurement system (PPMS) with a 14 T magnet and rotation stage (Quan-

tum Design).

SX-ARPES measurements were performed at the ADDRESS beamline of the Swiss Light Source. The samples were cooled down to 12–14 K in a transfer chamber with 10^{-10} mbar pressure, cleaved to expose a fresh surface, then transferred to an analysis chamber with 10^{-11} mbar pressure. The photon energy range used for Fig. 3 was 350–700 eV. The pass energy of the PHOIBOS-150 analyzer was set to 80 eV, and the corresponding angle-resolving mode was medium angle mode ($\pm 9^\circ$).

The experiment geometry is reported in the Supplemental Material of Ref. [14], along with the corresponding formulas used to determine the electron momentum. Corrections due to the incident photon momentum were taken into account. The conversion from photon energy $h\nu$ to momentum k_z was determined by assuming a free-electron-like final state, with inner potential chosen to match the experimentally observed band periodicity. These calculations were performed using the MATools code.

In addition to momentum-resolved measurements of the valence bands, we also performed XPS measurements of the core levels in NbS₂ [35]. Since the spectrum of a given core level exhibited shifts when taken at different photon energies due to an error in photon energy calibration, we made sure to correct these shifts by aligning to the Fermi edge of a valence band spectrum taken at the identical photon energy.

XPS spectra were processed and analyzed using the CASAXPS software. For the S 2*p* core level spectrum, we fitted the peaks to Gaussian-Lorentzian mixture functions on top of a Shirley background. We constrained the doublet spacing to the literature value of 1.18 eV [59] and the area ratio of the doublets to 1:2 (*p* orbitals). For the Nb 3*d* core level spectrum, we constrained the doublet spacing to 2.8 eV, which is within the range of values (2.7–2.9 eV [60, 61]) reported for NbSe₂, and the area ratio of the doublets to 2:3 (*d* orbitals). Due to the asymmetry in one of the peaks, we employed a Doniach-Sunjic line shape [62]. Photoionization cross sections were interpolated from theoretical computed values by Yeh and Lindau [63].

DFT calculations were performed using the CRYSTAL17 code [64]. The scalar relativistic pseudopotentials and the Gaussian-type basis functions are given in the Supplemental Material [35] (see, also, Refs. [65–67] therein). Spin-orbit coupling was not included, since the spin splitting is small compared to the experimental SX-

ARPES resolution. The mesh of *k*-points was determined by applying shrinking factors of 12 along *a** and *b** and 4 along *c**. This gives rise to 57 *k*-points in the irreducible part of the Brillouin zone. Starting from the experimental structure [43], all free parameters within the given space group, the lattice parameters *a* and *c*, as well as *z*(S), were relaxed until the root mean square on the gradient was below 0.0001 a.u. and the root mean square on the displacement was below 0.0004 a.u.

Atomic structures were visualized using VESTA [68].

APPENDIX B: TB MODEL

At $k_z = 0$, the eigenvalues of Eq. (2) can be solved analytically:

$$\epsilon_{\sigma_{\text{odd}}, \sigma_{\text{odd}}^*}(k_z = 0) = \epsilon_{p,\text{odd}} \pm t_{\perp}, \quad (4)$$

$$\epsilon_{\sigma_{\text{even1}}, \sigma_{\text{even1}}^*}(k_z = 0) = \frac{1}{2} \left[\epsilon_{p,\text{even}} + \epsilon_d \pm t_{\perp} - \sqrt{(\epsilon_{p,\text{even}} - \epsilon_d \pm t_{\perp})^2 + 4t_{\parallel}^2} \right], \quad (5)$$

and

$$\epsilon_{\sigma_{\text{even2}}, \sigma_{\text{even2}}^*}(k_z = 0) = \frac{1}{2} \left[\epsilon_{p,\text{even}} + \epsilon_d \pm t_{\perp} + \sqrt{(\epsilon_{p,\text{even}} - \epsilon_d \pm t_{\perp})^2 + 4t_{\parallel}^2} \right]. \quad (6)$$

From Eqs. (5) and (6), we can extract simple expressions for the bandwidths w_{even1} , w_{even2} in a few limiting cases. When there is no hybridization, i.e., $t_{\parallel} = 0$, the bandwidth of the S $3p_{z,\text{even}}$ states is $2t_{\perp}$ and that of the Nb $4d_{z^2}$ states is zero. When $\epsilon_{p,\text{even}} = \epsilon_d$ and t_{\parallel} is nonzero, $w_{\text{even1}} = w_{\text{even2}} = t_{\perp}$. When $(\epsilon_{p,\text{even}} - \epsilon_d \pm t_{\perp})^2 / 4t_{\parallel}^2 \ll 1$, we can apply a truncated binomial expansion to the square roots in Eqs. (5) and (6) and obtain

$$w_{\text{even1}}, w_{\text{even2}} \approx t_{\perp} \left[1 \mp \frac{\epsilon_{p,\text{even}} - \epsilon_d}{2t_{\parallel}} \right]. \quad (7)$$

From density functional theory (DFT) calculations, we have confirmed that $(\epsilon_{p,\text{even}} - \epsilon_d \pm t_{\perp})^2 / 4t_{\parallel}^2$ ranges from 0.004 to 0.23 and hence, the binomial approximation is reasonable here.

-
- [1] K. S. Novoselov, A. K. Geim, S. V. Morozov, D. Jiang, Y. Zhang, S. V. Dubonos, I. V. Grigorieva, and A. A. Firsov, Electric Field Effect in Atomically Thin Carbon Films, *Science* **306**, 666 (2004).
- [2] K. F. Mak, C. Lee, J. Hone, J. Shan, and T. F. Heinz, Atomically Thin MoS₂: A New Direct-Gap Semiconductor, *Phys. Rev. Lett.* **105**, 136805 (2010).

- [3] B. Huang, G. Clark, E. Navarro-Moratalla, D. R. Klein, R. Cheng, K. L. Seyler, D. Zhong, E. Schmidgall, M. A. McGuire, D. H. Cobden, W. Yao, D. Xiao, P. Jarillo-Herrero, and X. Xu, Layer-dependent ferromagnetism in a van der Waals crystal down to the monolayer limit, *Nature (London)* **546**, 270 (2017).

- [4] Z. Fei, T. Palomaki, S. Wu, W. Zhao, X. Cai, B. Sun, P. Nguyen, J. Finney, X. Xu, and D. H. Cobden, Edge conduction in monolayer WTe_2 , *Nat. Phys.* **13**, 677 (2017).
- [5] S. Tang, C. Zhang, D. Wong, Z. Pedramrazi, H.-Z. Tsai, C. Jia, B. Moritz, M. Claassen, H. Ryu, S. Kahn, J. Jiang, H. Yan, M. Hashimoto, D. Lu, R. G. Moore, C.-C. Hwang, C. Hwang, Z. Hussain, Y. Chen, M. M. Ugeda, Z. Liu, X. Xie, T. P. Devereaux, M. F. Crommie, S.-K. Mo, and Z.-X. Shen, Quantum spin Hall state in monolayer $1\text{T}'\text{-WTe}_2$, *Nat. Phys.* **13**, 683 (2017).
- [6] E. Cappelluti, R. Roldán, J. A. Silva-Guillén, P. Ordejón, and F. Guinea, Tight-binding model and direct-gap/indirect-gap transition in single-layer and multilayer mos_2 , *Phys. Rev. B* **88**, 075409 (2013).
- [7] S. Fang, R. Kuate Defo, S. N. Shirodkar, S. Lieu, G. A. Tritsarlis, and E. Kaxiras, *Ab initio* tight-binding Hamiltonian for transition metal dichalcogenides, *Phys. Rev. B* **92**, 205108 (2015).
- [8] S. Fang and E. Kaxiras, Electronic structure theory of weakly interacting bilayers, *Phys. Rev. B* **93**, 235153 (2016).
- [9] S. Carr, S. Fang, P. Jarillo-Herrero, and E. Kaxiras, Pressure dependence of the magic twist angle in graphene superlattices, *Phys. Rev. B* **98**, 085144 (2018).
- [10] R. S. Markiewicz, S. Sahrakorpi, M. Lindroos, H. Lin, and A. Bansil, One-band tight-binding model parametrization of the high- T_c cuprates including the effect of k_z dispersion, *Phys. Rev. B* **72**, 054519 (2005).
- [11] T. Ohta, A. Bostwick, J. L. McChesney, T. Seyller, K. Horn, and E. Rotenberg, Interlayer Interaction and Electronic Screening in Multilayer Graphene Investigated with Angle-Resolved Photoemission Spectroscopy, *Phys. Rev. Lett.* **98**, 206802 (2007).
- [12] C. W. Nicholson, C. Berthod, M. Puppini, H. Berger, M. Wolf, M. Hoesch, and C. Monney, Dimensional Crossover in a Charge Density Wave Material Probed by Angle-Resolved Photoemission Spectroscopy, *Phys. Rev. Lett.* **118**, 206401 (2017).
- [13] C. W. Nicholson, E. F. Schwier, K. Shimada, H. Berger, M. Hoesch, C. Berthod, and C. Monney, Role of a higher-dimensional interaction in stabilizing charge density waves in quasi-one-dimensional NbSe_3 revealed by angle-resolved photoemission spectroscopy, *Phys. Rev. B* **101**, 045412 (2020).
- [14] V. N. Strocov, M. Shi, M. Kobayashi, C. Monney, X. Wang, J. Krempasky, T. Schmitt, L. Patthey, H. Berger, and P. Blaha, Three-Dimensional Electron Realm in VSe_2 by Soft-X-Ray Photoelectron Spectroscopy: Origin of Charge-Density Waves, *Phys. Rev. Lett.* **109**, 086401 (2012).
- [15] V. Strocov, Intrinsic accuracy in 3-dimensional photoemission band mapping, *J. Electron Spectros. Relat. Phenomena* **130**, 65 (2003).
- [16] J. Wilson, F. D. Salvo, and S. Mahajan, Charge-density waves and superlattices in the metallic layered transition metal dichalcogenides, *Adv. Phys.* **24**, 117 (1975).
- [17] M. Naito and S. Tanaka, Electrical Transport Properties in $2H\text{-NbS}_2$, -NbSe_2 , -TaS_2 and -TaSe_2 , *J. Phys. Soc. Jpn.* **51**, 219 (1982).
- [18] I. Guillamón, H. Suderow, S. Vieira, L. Cario, P. Diener, and P. Rodière, Superconducting Density of States and Vortex Cores of $2H\text{-NbS}_2$, *Phys. Rev. Lett.* **101**, 166407 (2008).
- [19] M. Leroux, M. Le Tacon, M. Calandra, L. Cario, M.-A. Méasson, P. Diener, E. Borrisenko, A. Bosak, and P. Rodière, Anharmonic suppression of charge density waves in $2H\text{-NbS}_2$, *Phys. Rev. B* **86**, 155125 (2012).
- [20] R.-M. Stan, S. K. Mahatha, M. Bianchi, C. E. Sanders, D. Curcio, P. Hofmann, and J. A. Miwa, Epitaxial single-layer NbS_2 on $\text{Au}(111)$: Synthesis, structure, and electronic properties, *Phys. Rev. Materials* **3**, 044003 (2019).
- [21] M. Leroux, L. Cario, A. Bosak, and P. Rodière, Traces of charge density waves in NbS_2 , *Phys. Rev. B* **97**, 195140 (2018).
- [22] C. Wen, Y. Xie, Y. Wu, S. Shen, P. Kong, H. Lian, J. Li, H. Xing, and S. Yan, Impurity-pinned incommensurate charge density wave and local phonon excitations in $2H\text{-NbS}_2$, *Phys. Rev. B* **101**, 241404(R) (2020).
- [23] Y. Nishio, M. Shirai, N. Suzuki, and K. Motizuki, Role of Electron-Lattice Interaction in Layered Transition Metal Dichalcogenide $2H\text{-NbS}_2$. I. Phonon Anomaly and Superconductivity, *J. Phys. Soc. Japan* **63**, 156 (1994).
- [24] F. Güller, V. L. Vildosola, and A. M. Llois, Spin density wave instabilities in the NbS_2 monolayer, *Phys. Rev. B* **93**, 094434 (2016).
- [25] C. Heil, S. Poncé, H. Lambert, M. Schlipf, E. R. Margine, and F. Giustino, Origin of Superconductivity and Latent Charge Density Wave in NbS_2 , *Phys. Rev. Lett.* **119**, 087003 (2017).
- [26] C. Heil, M. Schlipf, and F. Giustino, Quasiparticle GW band structures and Fermi surfaces of bulk and monolayer NbS_2 , *Phys. Rev. B* **98**, 075120 (2018).
- [27] E. G. C. P. van Loon, M. Rösner, G. Schönhoff, M. I. Katsnelson, and T. O. Wehling, Competing Coulomb and electron-phonon interactions in NbS_2 , *npj Quantum Mater.* **3**, 32 (2018).
- [28] R. Bianco, I. Errea, L. Monacelli, M. Calandra, and F. Mauri, Quantum Enhancement of Charge Density Wave in NbS_2 in the Two-Dimensional Limit, *Nano Lett.* **19**, 3098 (2019).
- [29] D. Lin, S. Li, J. Wen, H. Berger, L. Forró, H. Zhou, S. Jia, T. Taniguchi, K. Watanabe, X. Xi, and M. S. Bahrany, Patterns and driving forces of dimensionality-dependent charge density waves in $2H$ -type transition metal dichalcogenides, *Nat. Commun.* **11**, 2406 (2020).
- [30] C.-w. Cho, J. Lyu, C. Y. Ng, J. J. He, K. T. Lo, D. Chareev, T. A. Abdel-Baset, M. Abdel-Hafiez, and R. Lortz, Evidence for the Fulde-Ferrell-Larkin-Ovchinnikov state in bulk NbS_2 , *Nat. Commun.* **12**, 3676 (2021).
- [31] V. N. Strocov, T. Schmitt, U. Flechsig, T. Schmidt, A. Imhof, Q. Chen, J. Raabe, R. Betemps, D. Zimoch, J. Krempasky, X. Wang, M. Grioni, A. Piazzalunga, and L. Patthey, High-resolution soft X-ray beamline ADDRESS at the Swiss Light Source for resonant inelastic X-ray scattering and angle-resolved photoelectron spectroscopies, *J. Synchrotron Radiat.* **17**, 631 (2010).
- [32] V. N. Strocov, X. Wang, M. Shi, M. Kobayashi, J. Krempasky, C. Hess, T. Schmitt, and L. Patthey, Soft-X-ray ARPES facility at the ADDRESS beamline of the SLS: concepts, technical realisation and scientific applications, *J. Synchrotron Radiat.* **21**, 32 (2014).
- [33] R. Yan, G. Khalsa, B. T. Schaefer, A. Jarjour, S. Rouvimov, K. C. Nowack, H. G. Xing, and D. Jena, Thickness dependence of superconductivity in ultrathin NbS_2 , *Appl. Phys. Express* **12**, 023008 (2019).
- [34] H. Lian, Y. Wu, H. Xing, S. Wang, and Y. Liu, Effect of stoichiometry on the superconducting transition tem-

- perature in single crystalline $2H$ -NbS₂, *Physica C Supercond.* **538**, 27 (2017).
- [35] See Supplemental Material at [URL will be inserted by publisher] for further XPS data, ARPES data with different photon polarizations, and DFT parameters and calculations.
- [36] Y. Saitoh, K. Kobayashi, A. Fujimori, Y. Yamamura, M. Koyano, T. Tsuji, and S. Katayama, Photoemission and core-level absorption spectroscopy of Fe_xNbS₂, *J. Electron Spectros. Relat. Phenomena* **144-147**, 829 (2005).
- [37] K. Onabe, M. Naito, and S. Tanaka, Anisotropy of Upper Critical Field in Superconducting $2H$ -NbS₂, *J. Phys. Soc. Jpn.* **45**, 50 (1978).
- [38] M. M. Ugeda, A. J. Bradley, Y. Zhang, S. Onishi, Y. Chen, W. Ruan, C. Ojeda-Aristizabal, H. Ryu, M. T. Edmonds, H.-Z. Tsai, A. Riss, S.-K. Mo, D. Lee, A. Zettl, Z. Hussain, Z.-X. Shen, and M. F. Crommie, Characterization of collective ground states in single-layer NbSe₂, *Nat. Phys.* **12**, 92 (2016).
- [39] F. Weber, R. Hott, R. Heid, L. L. Lev, M. Caputo, T. Schmitt, and V. N. Strocov, Three-dimensional Fermi surface of $2H$ - NbSe₂: Implications for the mechanism of charge density waves, *Phys. Rev. B* **97**, 235122 (2018).
- [40] N. Sirica, S.-K. Mo, F. Bondino, I. Pis, S. Nappini, P. Vilmercati, J. Yi, Z. Gai, P. C. Snijders, P. K. Das, I. Vobornik, N. Ghimire, M. R. Koehler, L. Li, D. Sapkota, D. S. Parker, D. G. Mandrus, and N. Mannella, Electronic structure of the chiral helimagnet and $3d$ -intercalated transition metal dichalcogenide Cr_{1/3}NbS₂, *Phys. Rev. B* **94**, 075141 (2016).
- [41] Z. El Youbi, S. W. Jung, C. Richter, K. Hricovini, C. Cacho, and M. D. Watson, Fermiology and electron-phonon coupling in the $2H$ and $3R$ polytypes of NbS₂, *Phys. Rev. B* **103**, 155105 (2021).
- [42] V. Strocov, Photoemission response of 2D electron states, *J. Electron Spectros. Relat. Phenomena* **229**, 100 (2018).
- [43] F. Jellinek, G. Brauer, and H. Müller, Molybdenum and Niobium Sulphides, *Nature* **185**, 376 (1960).
- [44] W. G. Fisher and M. J. Sienko, Stoichiometry, structure, and physical properties of niobium disulfide, *Inorg. Chem.* **19**, 39 (1980).
- [45] B. W. Pfalzgraf, H. Spreckels, W. Paulus, and R. Schollhorn, Order-disorder phase transition in layered Cu_{1/2}NbS₂ observed by electrical resistivity measurements, *J. Phys. F Met. Phys.* **17**, 857 (1987).
- [46] C. J. Carmalt, T. D. Manning, I. P. Parkin, E. S. Peters, and A. L. Hector, Formation of a new (1T) trigonal NbS₂ polytype via atmospheric pressure chemical vapour deposition, *J. Mater. Chem.* **14**, 290 (2004).
- [47] W. Wang, W. Lei, X. Zheng, H. Li, X. Tang, and X. Ming, Electronic structure and phase transition engineering in NbS₂: Crucial role of van der Waals interactions, *Chin. Phys. B* **29**, 056201 (2020).
- [48] J. P. Perdew, K. Burke, and M. Ernzerhof, Generalized Gradient Approximation Made Simple, *Phys. Rev. Lett.* **77**, 3865 (1996).
- [49] A. V. Krukau, O. A. Vydrov, A. F. Izmaylov, and G. E. Scuseria, Influence of the exchange screening parameter on the performance of screened hybrid functionals, *J. Chem. Phys.* **125**, 224106 (2006).
- [50] J. P. Perdew, A. Ruzsinszky, G. I. Csonka, O. A. Vydrov, G. E. Scuseria, L. A. Constantin, X. Zhou, and K. Burke, Restoring the Density-Gradient Expansion for Exchange in Solids and Surfaces, *Phys. Rev. Lett.* **100**, 136406 (2008).
- [51] L. Schimka, J. Harl, and G. Kresse, Improved hybrid functional for solids: The HSEsol functional, *J. Chem. Phys.* **134**, 024116 (2011).
- [52] S. Grimme, J. Antony, S. Ehrlich, and H. Krieg, A consistent and accurate ab initio parametrization of density functional dispersion correction (DFT-D) for the 94 elements H-Pu, *J. Chem. Phys.* **132**, 154104 (2010).
- [53] B. E. Brown and D. J. Beerntsen, Layer structure polytypism among niobium and tantalum selenides, *Acta Crystallogr.* **18**, 31 (1965).
- [54] M. Marezio, P. Dernier, A. Menth, and G. Hull, The crystal structure of NbSe₂ at 15°K, *J. Solid State Chem.* **4**, 425 (1972).
- [55] F. Levy and Y. Froidevaux, Structural and electrical properties of layered transition metal selenides V_xTi_{1-x}Se₂ and Ta_xTi_{1-x}Se₂, *J. Phys. C: Solid State Phys.* **12**, 473 (1979).
- [56] K. Hayashi and M. Nakahira, Stability and the equilibrium selenium vapor pressure of the VSe₂ phase, *J. Solid State Chem.* **24**, 153 (1978).
- [57] E. Kamil, J. Berges, G. Schönhoff, M. Rösner, M. Schüler, G. Sangiovanni, and T. O. Wehling, Electronic structure of single layer 1T-NbSe₂: interplay of lattice distortions, non-local exchange, and Mott-Hubbard correlations, *J. Phys. Condens. Matter* **30**, 325601 (2018).
- [58] A. Devarakonda, H. Inoue, S. Fang, C. Ozsoy-Keskinbora, T. Suzuki, M. Kriener, L. Fu, E. Kaxiras, D. C. Bell, and J. G. Checkelsky, Clean 2D superconductivity in a bulk van der Waals superlattice, *Science* **370**, 231 (2020).
- [59] J. Moulder and J. Chastain, *Handbook of X-ray Photoelectron Spectroscopy: A Reference Book of Standard Spectra for Identification and Interpretation of XPS Data* (Physical Electronics Division, Perkin-Elmer Corporation, 1992).
- [60] H. Wang, X. Huang, J. Lin, J. Cui, Y. Chen, C. Zhu, F. Liu, Q. Zeng, J. Zhou, P. Yu, X. Wang, H. He, S. H. Tsang, W. Gao, K. Suenaga, F. Ma, C. Yang, L. Lu, T. Yu, E. H. T. Teo, G. Liu, and Z. Liu, High-quality monolayer superconductor NbSe₂ grown by chemical vapour deposition, *Nat. Commun.* **8**, 394 (2017).
- [61] H. Lin, Q. Zhu, D. Shu, D. Lin, J. Xu, X. Huang, W. Shi, X. Xi, J. Wang, and L. Gao, Growth of environmentally stable transition metal selenide films, *Nat. Mater.* **18**, 602 (2019).
- [62] D. Morris, Y. Dou, J. Rebane, C. E. J. Mitchell, R. G. Egddell, D. S. L. Law, A. Vittadini, and M. Casarin, Photoemission and STM study of the electronic structure of Nb-doped TiO₂, *Phys. Rev. B* **61**, 13445 (2000).
- [63] J. Yeh and I. Lindau, Atomic subshell photoionization cross sections and asymmetry parameters: $1 \leq Z \leq 103$, *At. Data Nucl. Data Tables* **32**, 1 (1985).
- [64] R. Dovesi, A. Erba, R. Orlando, C. M. Zicovich-Wilson, B. Civalieri, L. Maschio, M. Rérat, S. Casassa, J. Baima, S. Salustro, and B. Kirtman, Quantum-mechanical condensed matter simulations with CRYSTAL, *WIREs Comput. Mol. Sci.* **8**, e1360 (2018).
- [65] D. Andrae, U. Häußermann, M. Dolg, H. Stoll, and H. Preuß, Energy-adjusted *ab initio* pseudopotentials for the second and third row transition elements, *Theor. Chim. Acta* **77**, 123 (1990).

- [66] A. Bergner, M. Dolg, W. Küchle, H. Stoll, and H. Preuß, *Ab initio* energy-adjusted pseudopotentials for elements of groups 13–17, *Mol. Phys.* **80**, 1431 (1993).
- [67] J. M. L. Martin and A. Sundermann, Correlation consistent valence basis sets for use with the Stuttgart–Dresden–Bonn relativistic effective core potentials: The atoms Ga–Kr and In–Xe, *J. Chem. Phys.* **114**, 3408 (2001).
- [68] K. Momma and F. Izumi, *VESTA3* for three-dimensional visualization of crystal, volumetric and morphology data, *J. Appl. Crystallogr.* **44**, 1272 (2011).
- [69] M. F. Peintinger, D. V. Oliveira, and T. Bredow, as implemented in CRYSTAL17, keyword POB-DZVPP.

SUPPLEMENTAL MATERIAL

Supplementary Note 1: X-ray Photoelectron Spectroscopy (XPS)

Figure S1(a) shows the survey spectrum with the expected core levels for Nb and S. Figure S1(b) shows the momentum-integrated valence band spectrum, which is qualitatively similar to that in Ref. [40].

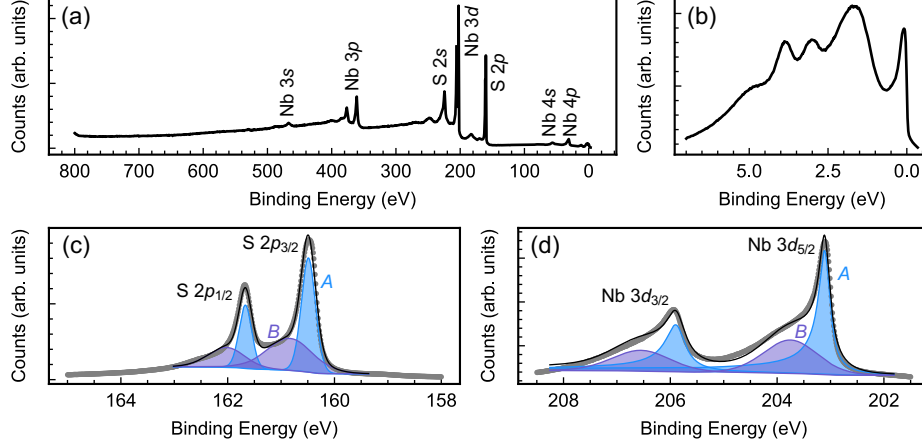


FIG. S1. XPS measurements of NbS₂. (a) Survey spectrum with prominent core levels labeled. (b) Valence band spectrum. (c) S 2p_{1/2} and 2p_{3/2} doublet. (d) Nb 3d_{3/2} and 3d_{5/2} doublet. In (c) and (d), the gray circles are the measured data, the black line is the overall fit, and the shaded areas are the individual peaks that constitute the fit. Photon energies: 1000 eV for (a), 402.5 eV for (b)–(d).

Figure S1(c) shows the spectrum of the S 2p_{1/2} and 2p_{3/2} doublet. Fit parameters are provided in Table S1. We observe that each doublet consists of two components, labeled *A* and *B*, indicating two species of S. This observation is reminiscent of XPS measurements in Fe_xNbS₂ [36], where the presence of the Fe intercalant creates two crystallographically inequivalent S sites. In those reports, the peak with lower binding energy (*A* in our case) was ascribed to S atoms in pristine sites of 2*H*-NbS₂, whereas the peak with higher binding energy (*B* in our case) was ascribed to S atoms coordinated with intercalants. The area ratio of the peaks was roughly consistent with the expected intercalant concentration *x*. For example, at *x* = 1/3, every S atom is coordinated with an intercalant, and hence the peak with lower binding energy was mostly suppressed.

TABLE S1. XPS fit parameters for the S 2*p* and Nb 3*d* core levels. GL(*p*) stands for a Gaussian-Lorentzian mixture function, where *p* is the mixing factor. *p* = 100 represents a pure Lorentzian, whereas *p* = 0 represents a pure Gaussian. DS(*a*) stands for the asymmetric Doniach-Sunjić line shape, where *a* is the asymmetry parameter. The area of each peak is reported as a percentage of the total area. FWHM stands for the full width at half maximum.

	S 2p _{3/2}		S 2p _{1/2}		Nb 3d _{5/2}		Nb 3d _{3/2}	
	S ^A	S ^B	S ^A	S ^B	Nb ^A	Nb ^B	Nb ^A	Nb ^B
Line shape	GL(30)	GL(30)	GL(30)	GL(30)	DS(0.15)	GL(30)	DS(0.15)	GL(30)
Area [%]	34.75	31.91	17.38	15.96	42.85	17.03	28.71	11.41
FWHM [eV]	0.31	1.02	0.28	0.82	0.24	1.19	0.43	1.27
Position [eV]	160.49	160.84	161.67	162.02	203.13	203.75	205.93	206.55

We thus may infer the presence of Nb intercalants in our measured NbS₂ crystals. As discussed in Ref. [34], during sample growth or annealing, Nb atoms that lose S may intercalate between layers. From the fits, we find that peak *A* (*B*) occupies 52% (48%) of the total area of the S 2*p* core spectra. Since every intercalant is coordinated with six neighboring S atoms, and each unit cell of 2*H*-NbS₂ consists of two NbS₂ layers, the concentration of Nb intercalants is one third of the fractional area occupied by peak *B*. Thus, we infer that our sample is Nb_{1+*x*}S₂, with a rough estimate of *x* ≈ 0.48/3 = 0.16.

Figure S1(d) shows the spectrum of the Nb 3d_{3/2} and 3d_{5/2} doublet. Again, each doublet is composed of two

components, labeled *A* and *B*, but *A* is clearly asymmetric, showing a long tail towards higher binding energies. Two possible interpretations exist for peaks *A* and *B*. They could represent two species of Nb, one within the NbS₂ layer, and the other as an intercalant. However, in both cases, the Nb atom is coordinated with six S atoms, so their local environment may be rather similar. Alternatively, there is some discussion of similar observations in Fe_xNbS₂ [36], Cr_{1/3}NbS₂ [40], and Nb-doped TiO₂ [62], where the observation of two components per Nb doublet does not indicate two Nb species, but a final-state screening effect. Essentially, the core hole produced during photoexcitation may pull down some localized *d* states below E_F , leading to a “well-screened” final state with asymmetric lineshape (*A*), in addition to the “poorly screened” final state with symmetric lineshape (*B*). To fit the asymmetric *A* peak, we employed a Doniach-Sunjic line shape [62].

The relative area ratio of the S 2*p* and Nb 3*d* core levels gives us another rough estimate of the stoichiometry. We computed the total area of the S 2*p* and Nb 3*d* peaks, then normalized by the theoretical photoionization cross sections computed by Yeh and Lindau [63]. The cross sections are dependent on photon energy, so for 402.5 eV, we performed cubic spline interpolation of the available tabulated data (Fig. S2) and estimated the cross sections to be 0.89 for S 2*p* and 3.1 for Nb 3*d*. This yields an *x* value of 0.14 for Nb_{1+x}S₂, which is close to our first estimate.

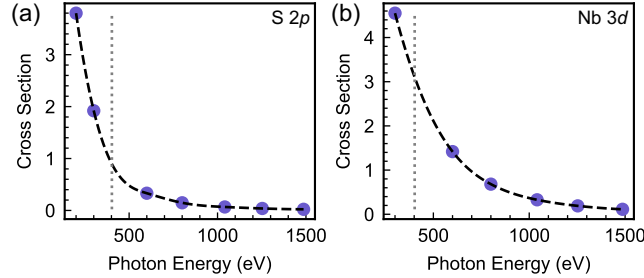


FIG. S2. XPS photoionization cross sections. The circles represent computed values by Yeh and Lindau [63] for (a) S 2*p* and (b) Nb 3*d* core levels. The black dashed lines represent cubic spline interpolations necessary to estimate the cross section at the photon energy used, 402.5 eV (gray dotted lines).

Supplementary Note 2: Photon Polarization Dependence

Figure S3 shows soft-x-ray angle-resolved photoemission spectroscopy (SX-ARPES) intensity cuts along Γ - K - M taken with circularly and linearly polarized photons. The different contrasts of the bands reflect their different orbital characters and are very similar to measurements on NbSe₂ [39]. Photons with linear vertical (LV) polarization, i.e., *p* polarization, pick out contributions from orbitals that are even with respect to the k_x - k_z plane, or with lobes extending out of the NbS₂ layer [38, 39]. Bands with enhanced intensity using LV photons include the k_z -dispersive bands at Γ (around -0.5 and -6 eV) and the near- E_F bands along Γ - K and at M , all of which contain dominant contributions from Nb 4*d*_{z²} and/or S 3*p*_z orbitals [Fig. S3(b)]. Photons with linear horizontal (LH) polarization, i.e., *s* polarization, pick out contributions from orbitals that are odd with respect to the k_x - k_z plane, or with lobes confined within the NbS₂ layer. Bands with enhanced intensity using LH photons include the k_z -nondispersive bands at Γ (around -1.5 and -2.5 eV), which contain dominant contributions from Nb 4*d*_{xz/yz}, Nb 4*d*_{xy/x²-y²}, and/or S 3*p*_{x/y} orbitals [Fig. S3(c)]. All bands are reasonably visible with circularly polarized (C) photons. Unless otherwise indicated, all reported SX-ARPES data were acquired with C polarization.

Supplementary Note 3: DFT

Tables S2 and S3 present computational details and parameters from the CRYSTAL17 code.

Structural parameters derived from full ionic relaxation are presented in Table S4, along with experimental values from literature.

Figures S4 and S5 show the various DFT calculations overlaying the SX-ARPES intensity along Γ - K - M [reproduced from Fig. 2(b)] and along Γ - A [reproduced from Fig. 3(a)]. Peaks in the energy distribution curves corresponding to the experimental bands are also overlaid to facilitate the comparison between experiment and theory. As discussed in the main text, the HSEsol calculation performs the best in reproducing the σ_{odd} , σ_{odd}^* bands near E_F . However, HSEsol appears to overshoot in lowering the energy of the σ_{even1} , σ_{even1}^* bands, and PBEsol gives a closer match to experiment [Fig. S5(c)]. From Fig. S4, we also note some trends at points in the Brillouin zone other than Γ

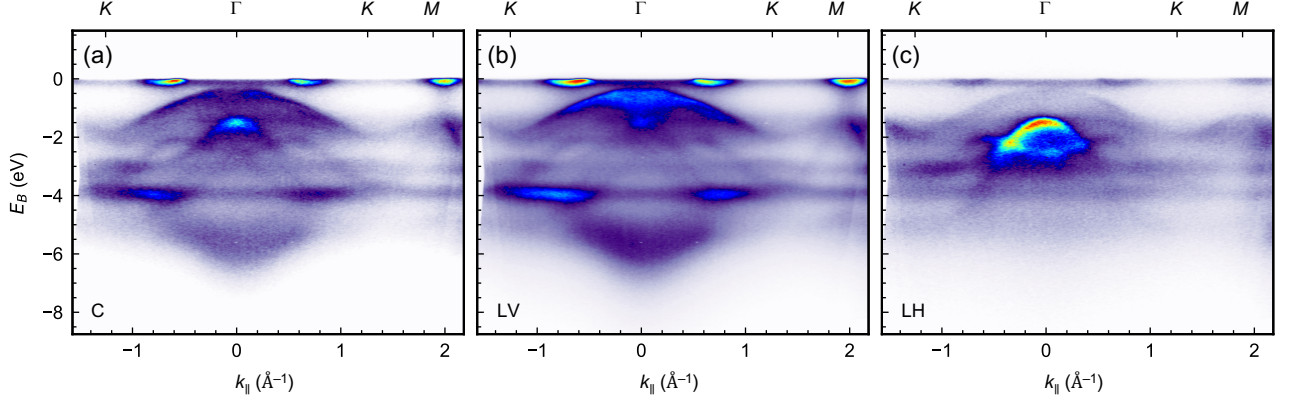


FIG. S3. Photon polarization dependence. SX-ARPES intensity cuts in the $k_z = 0$ plane using (a) circularly, (b) linearly vertically, and (c) linearly horizontally polarized photons. $h\nu = 590$ eV.

and A . The PBE-based functionals better reproduce the energy of the highest occupied state at K , but predict the highest occupied state at M to lie much closer to E_F than experiment. The hybrid functionals, HSE06 and HSEsol in particular, yield better predictions for the highest occupied state at M .

Supplementary Note 4: Dependence on Structural Parameters

To further elucidate the dependence of the electronic structure of NbS_2 on structural parameters, we computed the band structure with the HSEsol functional for four fixed values of c : 11.8, 12.2, 12.6, and 13.0 Å. The other atomic positions were allowed to relax. The structure with $c = 12.2$ Å has the lowest energy, and the energies relative to this structure are +14 meV, +11 meV, and +34 meV for the $c = 11.8, 12.6,$ and 13.0 Å structures, respectively. Fig. S6 shows the evolution of the fitted TB and structural parameters as a function of c . Consistent with Fig. 5 of the main text, the interlayer hopping t_\perp and bandwidth $w_{\text{even}1}$ show the greatest variation with c , while the orbital energy $\epsilon_{p,\text{odd}}$ and intralayer hybridization t_\parallel of even orbitals show the least variation. In terms of the atomic positions, d_{inter} increases as c increases, but d_{intra} retains a relatively constant value.

TABLE S2. Pseudopotentials (scalar relativistic) and basis sets.

Pseudopotential Core Valence Ref.	Nb		S	
	[Ar]3d ¹⁰ 4s ² 4p ⁶ 4d ³ 5s ² [65]		[Ne] 3s ² 3p ⁴ [66]	
	Exponent	Coefficient	Exponent	Coefficient
<i>s</i> -shell	6.566301	-0.8582654	6.833518	-0.043875
	4.586438	1.3041672	2.077738	0.319894
	3.753770	0.5069043	0.419121	-0.661233
	0.889871	1.0	0.153237	1.0
	0.407138	1.0		
	0.094271	1.0		
<i>p</i> -shell	3.070063	-3.9044315	1.817139	-0.079227
	2.237964	4.0688070	0.855070	0.263671
			0.312053	0.580682
	0.852255	0.6713910		
	0.504436	0.3474365	0.101687	1.0
	0.2668	1.0		
<i>d</i> -shell	0.09	1.0		
	4.053563	-0.0204201	0.2628 [69]	1.0
	1.652600	0.2089854		
	0.706859	0.4705515	0.11	1.0
	0.286367	0.4758860		
<i>f</i> -shell	0.108757	1.0		
	0.97 [67]	1.0		
	0.261	1.0		

TABLE S3. Tolerance and other computational parameters used in the CRYSTAL17 input.

TOLINTEG	12 12 12 12 24
TOLPSEUD	12
TOLDEE	8
BIPOLAR	64 64
LEVSHIFT	6 0

TABLE S4. Structural parameters from DFT calculations and experiments.

	PBE	PBE +D3	PBEsol	PBEsol +D3	HSE06	HSE06 +D3	HSEsol	HSEsol +D3	Expt. 1	Expt. 2	Expt. 3	Expt. 4
a (Å)	3.362	3.319	3.318	3.280	3.340	3.291	3.312	3.279	[43]	[44]	[45]	[46]
c (Å)	12.988	11.690	11.901	11.34	12.861	11.581	12.186	11.485	11.89	11.95	12.00	11.860
$z(S)/c$	0.128	0.116	0.117	0.111	0.128	0.115	0.122	0.114	0.125	0.108	0.125	0.1079

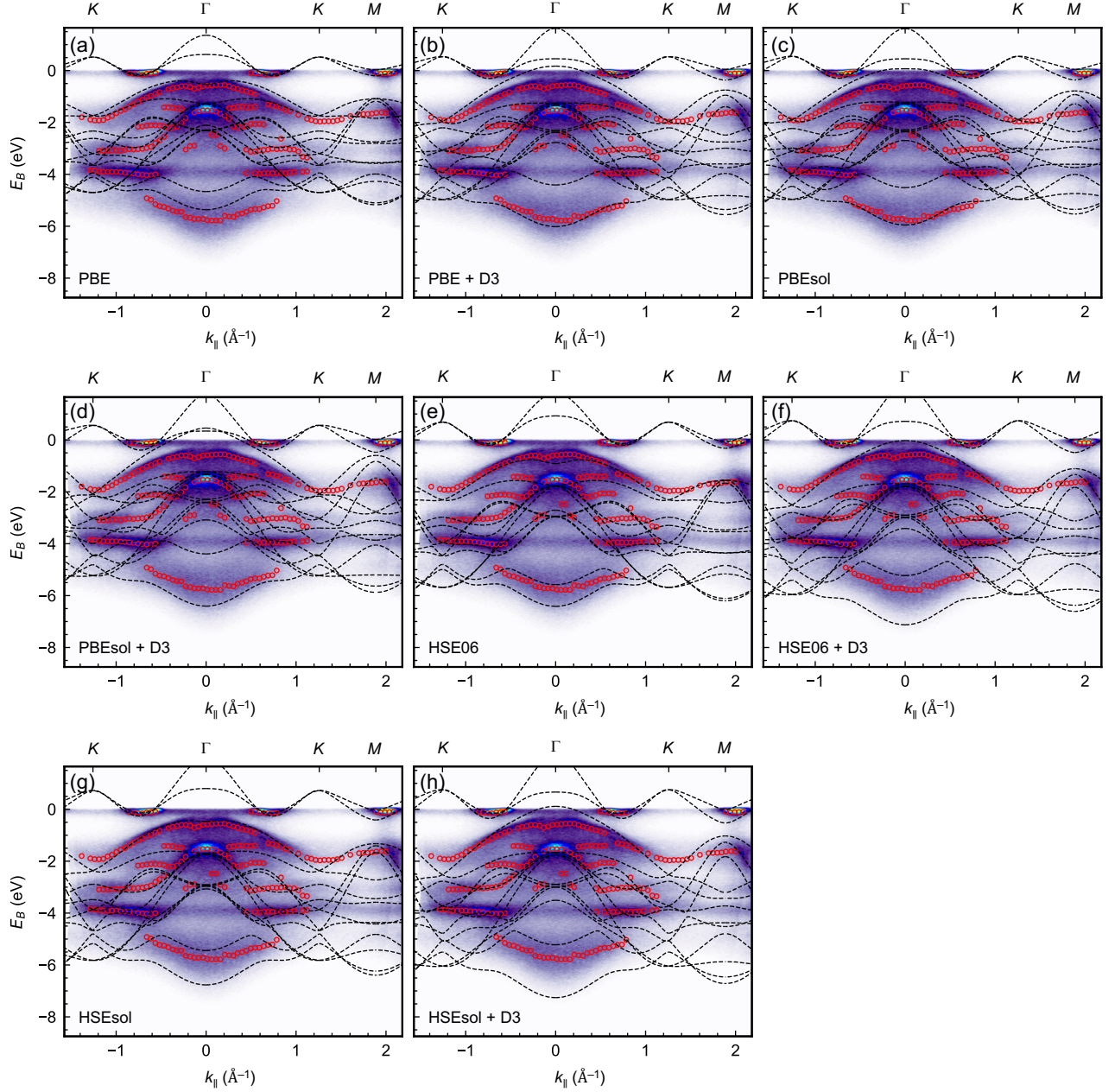


FIG. S4. Comparison of DFT calculations using different exchange-correlation and hybrid functionals along Γ - K - M . The open circles overlaying the experimental SX-ARPES intensities represent local peaks detected in the energy distribution curves, whereas the dashed lines represent the different DFT calculations. $h\nu = 590$ eV.

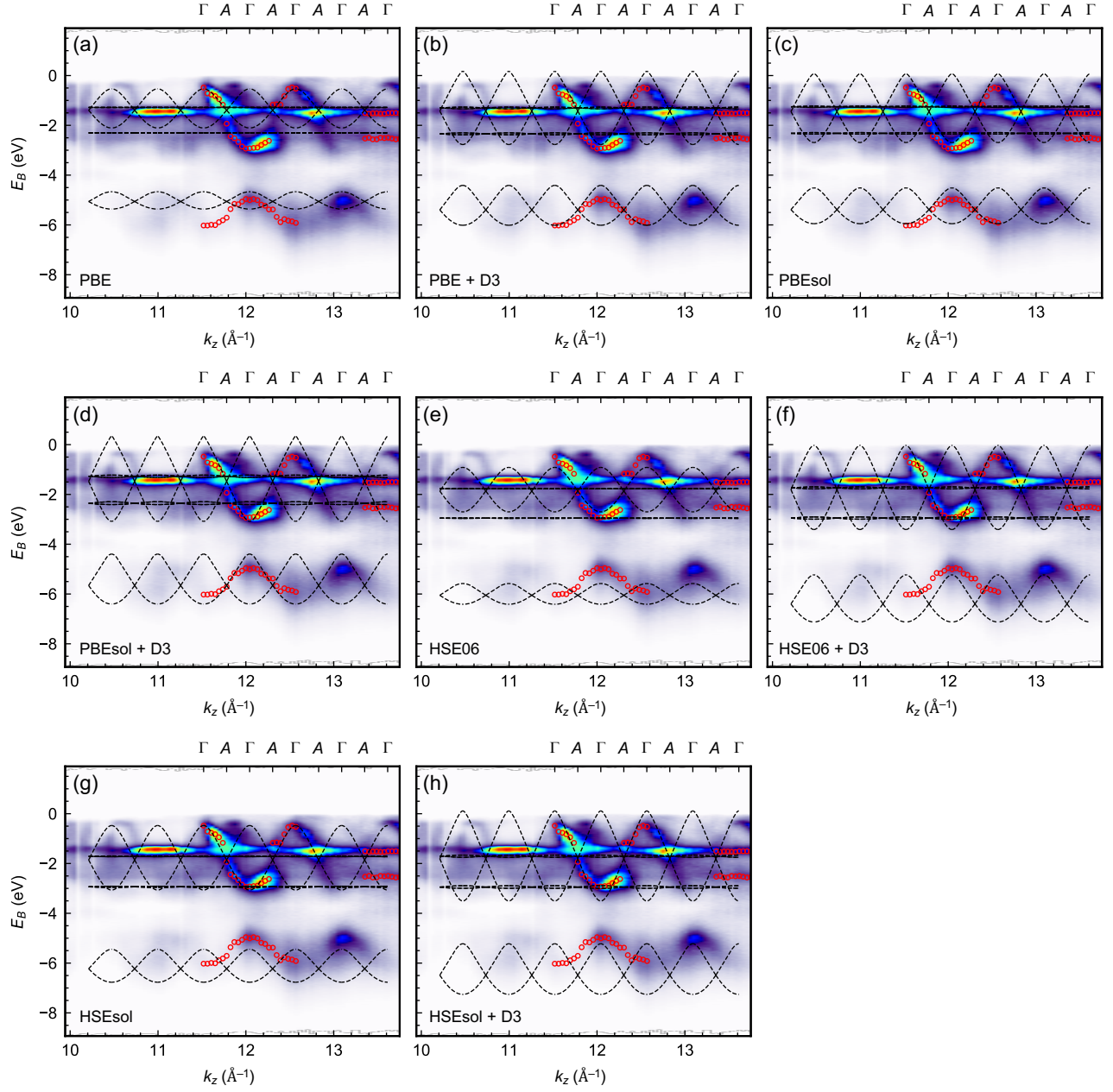


FIG. S5. Comparison of DFT calculations using different exchange-correlation and hybrid functionals along Γ -A. The open circles overlaying the experimental SX-ARPES intensities represent local peaks detected in the energy distribution curves, whereas the dashed lines represent the different DFT calculations.

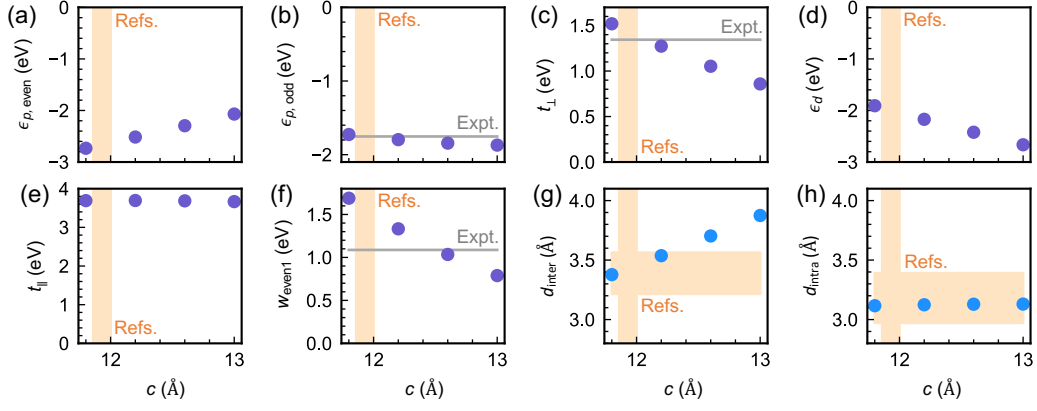


FIG. S6. Evolution of TB and structural parameters as a function of the c lattice constant. The DFT band structures with the HSEsol functional are computed for $c = 11.8, 12.2, 12.6,$ and 13.0 Å, then fitted to the TB model. Experimental values extracted from SX-ARPES are depicted as gray horizontal lines. The spread of structural parameters reported in literature [43–46] is marked by the shaded orange regions.